GEOPHYSICS®

Sparse laterally constrained inversion of surface wave dispersion curves via minimum gradient support regularization

Journal:	*Geophysics*
Manuscript ID	GEO-2021-0247.R2
Manuscript Type:	Technical Paper
Keywords:	surface wave, inversion, near surface
Manuscript Focus Area:	Seismic Inversion, Geophysical Software and Algorithms

DOI:10.1190/geo2021-0247.1

DOI: 10.1190/geo2021-0247.1

Sparse laterally constrained inversion of surface wave dispersion curves via minimum gradient support regularization

Julien Guillemoteau[*], **Giulio Vignoli** [†§], **Jeniffer Barreto**[†], **Guillaume Sauvin**[‡]

[*] *Universität Potsdam, Institut für Geowissenschaften, Karl-Liebknecht-Strasse 24, 14476 Potsdam-Golm, Germany.* [†] *University of Cagliari, 09123 Cagliari, Italy.* [‡] *Norwegian Geotechnical Institute (NGI), 0855, Oslo, Norway.* [§] *Geological Survey of Denmark and Greenland, 8000 Aarhus, Denmark.*

(February 7, 2022)

Corresponding author (Julien G.): julien@geo.uni-potsdam.de

Running head: **Sparse LCI of surface wave data**

ABSTRACT

We present a 1D laterally constrained inversion of surface wave dispersion curves based on the minimum gradient support regularization, which allows solutions with tunable sharpness in both vertical and horizontal directions. The forward modelling consists of a finite elements approach incorporated in a flexible non-parametric gradient-based inversion scheme, which has already demonstrated good stability and convergence capabilities when tested on other kinds of data. Our deterministic inversion procedure is performed in the shear-wave velocity log-space as we noticed that the associated Jacobian shows a reduced model dependency, and this, in turn, decreases the risks of local non-convexity. We show several synthetics and one field example to demonstrate the effectiveness and the applicability of the proposed approach.

DOI: 10.1190/geo2021-0247.1

INTRODUCTION

A common approach for the deterministic inversion of surface wave dispersion curves is to use a fixed 1D vertical discretization for the subsurface model. In this case, the stability and uniqueness of the 1D inverse problem are usually guaranteed via the application of Occam-type (minimum gradient norm) regularization constraints (Xia et al., 1999). An important side effect of such a regularization, however, is that sharp interfaces can no longer be accurately characterized as smooth models are promoted (Haney and Tsai, 2017). A possible strategy to address this issue consists of inverting for a few layers with variable thickness (Wang and Teng, 1994; Farrugia et al., 2016). Nevertheless, in the case of large surveys composed of hundreds to thousands dispersion curves (Halliday et al., 2010; Vignoli et al., 2012), the selection of a particular and constant number of layers can be equally problematic. Recently, several approaches relying on different regularization schemes have been proposed to allow more effective reconstructions when vertical abrupt velocity changes are present. For example, Haney and Qu (2010), and Esfahani et al. (2020) discuss the advantages of regularization terms consisting of the L1-norm, rather than the more standard L2-norm stabilizer. On the other hand, Vignoli et al. (2021) demonstrates the effectiveness of regularization based on Minimum Gradient Support (MGS) stabilizer. In particular, in the present research, we further develop the MGS inversion of surface wave data by addressing the problems connected, not only with the vertical sharp velocity changes, but also with the crucial issue of abrupt lateral variations. Indeed, precise reconstruction of the lateral velocity changes is important for a wide range of applications spanning, for example, from geological/geotechnical characterization (Bergamo et al., 2012; Craig et al., 2021) and oil and mineral exploration (Vignoli et al., 2011; Da Col et al., 2020), to reliable seismic site response assessment (Boaga et al., 2012). Very often, in the attempt of retrieving 2D/3D

DOI: 10.1190/geo2021-0247.1

shear-wave velocity distributions, adjacent dispersion curves are inverted individually and simply stitched together afterwards (Vignoli et al., 2016). This approach is generally justified by the fact that, because the physics of the method and the implicit lateral averaging for the dispersion curve extraction, nearby dispersion curves cannot be too different even when the geology is. However, for example, in the (to a large extent, similar) case of electromagnetic signals, mutually constraining close by soundings has been proved to be effective in enforcing lateral consistency and further reducing unwanted artefacts. In these cases, by still using 1D forward modelling, multiple adjacent soundings are jointly inverted with a stabilizing term bounding the corresponding 1D models laterally. This is the essence of the 1D Laterally Constrained Inversion (LCI), developed initially in the framework of electric (Auken et al., 2005) and electromagnetic methods (Auken and Christiansen, 2004), and, later, applied also to surface wave data (Wisén and Christiansen, 2005; Socco et al., 2009). The original LCI algorithms select solutions that are laterally smooth (in the sense of the L2-norm inversion), preventing the reconstruction of blocky structures characterized by constant physical parameters. To cope with this, MGS regularizations have been successfully tested on LCI schemes for the interpretation of electromagnetic data (Vignoli et al., 2015, 2017). In a similar line of reasoning, in the present research, we discuss the implementation of a LCI-MGS algorithm for the sparse inversion of the seismic surface wave dispersion curves. In particular, we first discuss the theoretical framework and the implementation details; then, we analyse the performances on synthetic and experimental data collected on a Norwegian test site.

DOI: 10.1190/geo2021-0247.1

METHODS

Formulation of the inverse problem

By assuming homogeneous Poisson's ratio and density, the Jacobian operator, locally connecting the phase velocities $\mathbf{c}$ and the subsurface shear-wave velocities $\boldsymbol{\beta}$, can be expressed by (Haney and Tsai, 2017)

$$J_{ij} = \frac{\delta c_i}{\delta \beta_j} = K^c_{\beta,ij} \frac{c_i}{\beta_j}, \tag{1}$$

where $K^c_{\beta,ij}$ is the phase-velocity kernel for a shear-wave velocity, which is twice the sum of the kernels for the shear-modulus μ and the Lamé first parameter λ:

$$K^c_{\beta,ij} = 2(K^c_{\mu,ij} + K^c_{\lambda,ij}). \tag{2}$$

A homogeneous Poisson's ratio is reasonable for deep investigations (Xing et al., 2016; Esfahani et al., 2020), while, for shallower studies, the saturation might affect P-wave velocity (and, in turn, on Poisson's ratio); in these cases, for example, the depth of the water-table should be taken into account for the proper assessment of the Poisson's ratio variability (Foti and Strobbia, 2002). For sake of simplicity, in the the present manuscript, all the examples and tests are performed with the hypothesis of homogeneous mass density and constant Poisson's ratio; extensions based on other assumption should not invalidate our conclusions. The problem of inverting phase velocity data to reconstruct a shear-wave subsurface model is highly non-linear as clearly shown by Equation 1 where the Jacobian is explicitly dependent on the β velocities (note that in addition, $K^c_{\beta,i,j}$ is also dependent on $\boldsymbol{\beta}$). This can be a source of local non-convexity of the inverse problem making gradient-based nonlinear inversion approaches likely sensitive to the starting model. Regarding this aspect, we noted that the Jacobian associated to a shear-wave velocity model in the log-space show

a reduced model dependency as explicitly shown here

$$G_{ij} = \frac{\delta c_i}{\delta \log \beta_j} = \beta_j J_{ij} = K^c_{\beta,ij} c_i, \tag{3}$$

where the term log stands for the natural logarithmic function (basis e). In Figure 1 a-b, we illustrate this aspect by comparing the original Jacobian $J = \partial c/\partial \beta$ and the new $G = \partial c/\partial log\beta$ for two local perturbations of a homogeneous medium. Following this observation, and in the attempt to reduce at best the likeliness of local non-convexity of the inverse problem, we suggest an inversion procedure with a model space corresponding to the logarithm of the shear-wave velocities. To do so, we use the OCCAM iterative procedure introduced by Constable et al. (1987), which for our case takes the form (Aster et al., 2005):

$$\begin{aligned} \log \boldsymbol{\beta}^{(n+1)} = &\left[\mathbf{G}^{(n)T}\mathbf{W_d}\mathbf{G}^{(n)} + \alpha_n \mathbf{W_m}\right]^{-1} \mathbf{G}^{(n)T}\mathbf{W_d} \\ &\left[\mathbf{c} + \mathbf{G}^{(n)} \log \boldsymbol{\beta}^{(n)} - \mathbf{f}(\log \boldsymbol{\beta}^{(n)})\right] \end{aligned} \tag{4}$$

where $\mathbf{W_d}$ is a diagonal matrix containing the the squared inverse of the data uncertainty, $\mathbf{f}(\log \boldsymbol{\beta}^{(n)})$ is the full forward modelling of the problem at iteration n, $\mathbf{W_m}$ is the matrix formalizing the adopted model regularization and α_n is the coefficient controlling the importance of the regularization term with respect to the data misfit. Similarly to Constable et al. (1987) and Key (2016), the α_n value is automatically defined at each iteration by analysing the χ square or Root Mean Square (RMS) misfit function, which we note $\phi_n(\alpha)$ for a broad range of α values. In practice, at iteration n, our algorithm starts with the largest α value and decreases it until $-d\phi/d\alpha > 0$ for which we set $\alpha_n = \alpha$. An example of such iterative α_n selection is given in Figure 1c. This iterative procedure is stopped if the change in misfit with respect to the previous iteration, is positive or shows an absolute value below 2.5 10^{-4}.

Finite elements based inversion

We compute $\mathbf{f}(\log \boldsymbol{\beta}^{(n)})$ and the elements $G_{ij}^{(n)}$ in equation 4 using the 1D finite elements (FE) approach discussed in Haney and Tsai (2017) and based on Lysmer (1970). In the context of inversion, for which we don't know the velocity model in advance, it is difficult to optimally set the 1D grid according the basic rules of thumbs associated to the FE methods (minimum size of the layers, minimum total extent of the grid). To ensure good precision and stability of the FE forward modelling during inversion, we use a rather fine homogeneous grid with a rather large maximum extent (2-3 times the largest apparent wavelength of the observed $\mathbf{c}$ curve). However, even for (non-parametric) grid-based deterministic inversion, we may not wish such a fine grid as it would result in a excessive number of parameters, hence resulting in rather large matrices to be inverted. We may also use heterogeneous layer thickness (e.g., increasing with depth), which may be an optimal choice for efficiently inverting dispersion curves recorded over a broad frequency range, and various subsurface velocity settings (e.g., when simultaneously inverting a full profile). Finally, we may use few layers only as for the case of a deterministic parametric inversion. In order to make our approach flexible in all these situations, we decouple the parameter grid used for the inversion from the FE grid used to compute the dispersion curves and the Jacobians. To do so, we define the layers j used for inversion as composed of a specific number of finite element sub-layers k as follows (see also Figure 1d)

$$\beta_k^{(n)} = \beta_j^{(n)}, \;\; k \in [a_j, b_j], \tag{5}$$

where a_j and b_j are the first and last element of the j^{th} layer in the finer finite element grid. Accordingly, the elements of the Jacobian matrix are given by

$$G_{ij}^{(n)} = \beta_j^{(n)} \sum_{k=a_j}^{k=b_j} J_{ik}^{(n)}. \tag{6}$$

Minimum gradient support for model regularization

The original procedure presented in Constable et al. (1987) aimed at providing the smoothest model fitting the data. Following this approach, in the LCI case, the model regularization matrix is given by

$$\mathbf{W_m} = \mathbf{D}_z^T \mathbf{D}_z + \mathbf{D}_x^T \mathbf{D}_x \tag{7}$$

where the matrices $\mathbf{D}_z$ and $\mathbf{D}_x$ are first or second order differential operator applied to neighbouring model elements in vertical and horizontal direction, respectively. The smoothest model is always worth being considered without prior information as it is a cheap conservative solution preventing overestimation of the imaging resolution (Constable et al., 1987).

In this study, our aim is to provide a tool allowing the rapid generation of solutions having different levels of sharpness. Clearly, the proposed approach inherits all the limitations of the deterministic approaches. In this respect, for example, stochastic methods (Wathelet et al., 2004; Wathelet, 2008) can be by far more exhaustive. However, a deterministic strategy to investigate the solution space by enforcing different levels of sparsity and highlighting different features at different scale can be seen as an intermediate tool between the computationally very efficient deterministic inversion and the relatively expensive stochastic approaches. Thus, to control the model sharpness, we use the following model regularization operator which consists in un-weighting the smoothness constraints in some local areas of the model space:

$$\mathbf{W_m} = \mathbf{S}_z^T \mathbf{S}_z + \gamma \mathbf{S}_x^T \mathbf{S}_x \tag{8}$$

where γ is a scalar value controlling the level of lateral constraint, and the elements of $\mathbf{S}$

are

$$S_{z,ij} = \frac{D_{z,ij}}{\sqrt{\eta_{z,j}^2 + \epsilon^2}}, \quad S_{x,ij} = \frac{D_{x,ij}}{\sqrt{\eta_{x,j}^2 + \epsilon^2}} \tag{9}$$

Here, the vectors $\boldsymbol{\eta}$ are functions allowing to locally decrease the smoothness constraints in the model space and ϵ is a stabilizer for the cases $\eta_j = 0$. Such $\boldsymbol{\eta}$ functions have been used with different strategies. Brown et al. (2012) used seismic velocity gradients and Yan et al. (2017) used seismic reflection to constrain the inversion of geo-electric data. In this study, we consider the case of an unconstrained inversion and follow the Minimum Gradient Support (MGS) regularization introduced by Portniaguine and Zhdanov (1999), which consists in sharpening the solution at every iteration n, by taking $\boldsymbol{\eta}$ equal to the gradient of the solution at the preceding iteration:

$$\boldsymbol{\eta}_z = \mathbf{D}_z \log \boldsymbol{\beta}^{(n)}, \quad \boldsymbol{\eta}_x = \mathbf{D}_x \log \boldsymbol{\beta}^{(n)} \tag{10}$$

As discussed in Vignoli et al. (2015) and Vignoli et al. (2021), the parameter ϵ can also be seen as a factor modulating the influence of the above model on the denominator of equation 9. Indeed, for large values i.e., $\epsilon \gg \mathbf{D} \log \boldsymbol{\beta}^{(n)}$, the regularization is equivalent to the Occam regularization (Constable et al., 1987; deGroot Hedlin and Constable, 1990; Key, 2016), while for values fulfilling $\epsilon \leq \mathbf{D} \log \boldsymbol{\beta}^{(n)}$, the amplitude of the smoothness "de-weighting", as well as the number of parameters affected by this de-weighting is tuned by the value of ϵ.

Vignoli et al. (2021) propose a practical criterion for the choice of ϵ and use this parameter to define the threshold discriminating between small and large velocity variations in order to investigate features at different scales. Here, it is worth noting the benefit of using the logarithmic space shear waves velocities parametrization, also in the framework of the MGS regularization. Indeed, by considering the logarithm of the shear-wave velocities, the

DOI: 10.1190/geo2021-0247.1

scale-dependency of the MGS operator is automatically removed and, in principle, the same range of ϵ values can be used to explore the sharpness of the solutions no matter if we are dealing with problems at crustal scale or data collected for near-surface characterizations.

RESULTS

Synthetic single sounding inversion tests

In order to better illustrate the most basic features of our inversion procedure, we first present a synthetic experiment considering the vertically constrained inversion (VCI) of a single sounding curve. For this test, we select a subsurface layered shear-wave model similar to one discussed in Esfahani et al. (2020), with homogeneous α/β ratio and density relationship parameters (see Table **??**).

The synthetic $\mathbf{c}$ data are computed for frequencies between 4 Hz and 50 Hz with a step of 2 Hz using a FE grid 200 m deep and and characterized by 0.2 m thick layers. During the inversion, as described by Equations 5-6 and Figure 1d: i) for the forward modelling $\boldsymbol{f}(log\boldsymbol{\beta}^{(n)})$ and the associated calculation of the Jacobian J_{ik}, the same, fine, FE discretization has been used, whereas, ii) for the actual inversion parameterization, the FE discretization has been remapped into coarser ones (100 and 550 layers). We define the starting model as a homogeneous model of velocity equal to the mean of the dispersion curve

$$\boldsymbol{\beta}^{(n=0)} = \bar{\mathbf{c}}. \tag{11}$$

We first perform a noise-free synthetic experiment. For this test, we set a fictitious uncertainty level of 1% and a very small χ-square value of 0.005 in order to force the algorithm to fit the data as much as it can. In Figure 2, we show the results for two

different parameter grids. The first is a rather dense grid of 550 layers with constant layer thicknesses; the second one is coarser with increasing thicknesses. Firstly, we see that both inversions show a final mean χ value in the range 0.01, i.e., corresponding to a fit of around 0.01%, which is largely acceptable according to what is needed in most of the practical situations. Both grids allow an effective reconstruction of the true model via the MGS regularization with epsilon value of 0.001 (Figure 2a). The inversion with the fine homogeneous grid steadily converges across a larger number of iteration than the inversion with the coarse heterogeneous grid. This is expected from the fact the fine grid gives more model freedom for the algorithm to reconstruct the model almost perfectly.

We perform a second single sounding inversion experiment for noisy synthetic data, by using the heterogeneous grid analysed above, and by testing two extreme values for ϵ. For this tests, uncorrelated $\pm 5\%$ random noise was added to the dispersion curve. For the inversions, we set a constant standard deviation value of 5% and a very small χ value for the same purpose as the first experiment. The results are shown in Figure 3. We see that both inversions reach the desired misfit and provide consistent solutions, which are a sharp model for $\epsilon = 0.001$, and a smooth model for a large value $\epsilon = 1$.

We finally apply this single sounding VCI approach to a pseudo-2D profile composed of dispersion curves, computed for 50 layered models, which are stitched together afterwards. The true layered models consist of the same 4 layers as the ones considered for the previous VCI test (described in Table **??**), but with laterally varying thicknesses as shown in Figure 4. This synthetic pseudo-2D data set was computed with the same FE parametrization as for the previous VCI test. Similarly, we added uncorrelated random noise in the range $\pm 5\%$ to each data point. We use the same inversion setup as for the previous test. In Figure 5, we show the results for four values of ϵ. For the sake of consistency with the real data case

discussed later (for which we don't have data uncertainty values), we now show and analyse the data misfits in term of relative root mean square (RMS) errors (a χ square analysis requires prior uncertainties). In any case, it is clear from Figure 5a and b that all the four experiments mostly fit the data within the error bars with comparable distributions, and by this fact show a stable sounding misfit level (of around 3 % in Figure 5b) while showing models with different sharpness (Figure 5c). This highlights how non-unique is the inverse problem and motivate the use of various sharpness. When looking in more details at each pseudo-section, we see rather high lateral variability of the solution. Our inversion procedure theoretically prevent over-fitting (this is well-demonstrated by Figure 3) by including the information about the expected noise level in the inversion. Due to this characteristic, a data over-fitting cannot be considered as the main cause of such variations. These kind of lateral oscillations are actually recognizable in other examples of pseudo-2D reconstructions based on 1D forward modelling and concerning other types of geophysical data (Auken and Christiansen, 2004; Auken et al., 2005). These lateral instabilities in the solution are connected with the ill-posedness of the 1D inversion in presence of noisy measurements and a finite number of available observations. If using single sounding inversions, such effect can only be avoided by laterally smoothing the data or by under-fitting the data. However, both of such operations may cause a loss in imaging resolution.

Synthetic multi-soundings LCI inversion tests

For the next synthetic tests, we consider the simultaneous 1D inversions of 50 dispersion curves using bi-directional MGS constraints. By definition, such multi-soundings 1D inversion do not provide physically-based relations for modelling either the lateral variations of the models nor the lateral variations of the noise. In this respect, a 1:1 balance between the

vertical and lateral constraints is not likely to be adapted for every case depending on the subsurface velocities and the spatial sampling of the profiles. That's why, in the presented inversion procedure, we suggest a lateral weight γ in equation 8 to compensate such effect. In practice, γ can be easily adjusted by looking the result of the first iteration. We proceed as follows: if the first iteration solution is significantly smoother than the lateral distribution of the dispersion curves, this means that γ is too large, conversely if such solution show an erratic lateral distribution, similar to some guessed noise feature, then γ should be increased. This operation is done manually as it required typically 4-5 tests only.

Similarly to the single sounding test, we take the starting models as a set of 50 homogeneous 1D models with a shear-wave velocity equal to the mean of the associated dispersion curves. This choice has important practical consequences as, for the first iteration, the vertical MGS operator has a denominator with a vector η_z homogeneously zero, which induces implicit weighting of $1/\epsilon_z^2$. For the case $\epsilon_z = 0.001$, this corresponds to 10^6 over-balancing in favour of the vertical constraints. To avoid this effect, for the first iteration, and more generally if one of the vectors $\boldsymbol{\eta}$ (equation 10) contains zero values only, each regularization matrix is normalized by the sum of its diagonal.

$$\mathbf{W_m}^{(n=0,\boldsymbol{\eta}=\mathbf{0})} = \frac{\mathbf{S}_z^T\mathbf{S}_z}{\sum diag(\mathbf{S}_z^T\mathbf{S}_z)} + \frac{\gamma\mathbf{S}_x^T\mathbf{S}_x}{\sum diag(\mathbf{S}_x^T\mathbf{S}_x)} \tag{12}$$

For the following iterations, where model gradients shows non-zeros values, we don't perform such balancing in order to ensure a rather "natural" or self-induced model-dependent iterative sharpening effect. In practice, we scale nevertheless the complete regularization term by the sum of the diagonal elements of one MGS matrix (we take the z-direction). This is done to facilitate the α-search described above as it ensures that the optimal α_n lies

in a relatively narrow range:

$$\mathbf{W_m}^{(n\geq 1,\boldsymbol{\eta}\neq\mathbf{0})} = \frac{1}{\sum diag(\mathbf{S}_z^T\mathbf{S}_z)}\left[\mathbf{S}_z^T\mathbf{S}_z + \gamma\mathbf{S}_x^T\mathbf{S}_x\right]. \tag{13}$$

The results of the LCI-MGS inversion is shown in Figure 6 for four values of ϵ, hence providing models characterized by similar data misfits, but varying sparsity levels. We can see that the LCI inversion removes the lateral oscillations observed in the previous single sounding inversions case without compromising the data fitting performances. This example illustrates the benefit of using lateral constraints and demonstrate the possibility to provide the resulting pseudo-2D models with different degrees of sharpness.

Field data example: The Vålen quick clay test site

In this section, we apply the proposed inversion scheme to real surface wave data from a quick clay research site in Norway (Sauvin et al., 2011). Quick clay may be described as highly sensitive marine clay that changes from a relatively stiff condition to a liquid mass when disturbed. Extended quick clay layers account for a lot of geo-hazards in Scandinavia and North-America and hence their occurrence and extent need to be mapped.

The Vålen site is located near the town of Vestfossen, approximately 65 km south-west of Oslo (Figure 7a). As a marine clay deposit in coastal, post-submarine area, this test site of the Norwegian Geotechnical Institute (NGI) is subject to quick clay landslides. Motivated by positive results obtained in similar area (Pfaffhuber et al., 2010), a geophysical survey including seismic measurements for Multichannel Analysis of Surface Waves (MASW) was performed in summer 2010 to better constrain the whole geological setting. The expected quick-clay layers are targeted to check their geophysical/geotechnical response to the different measurement techniques adopted. Here, we only consider the MASW data to test out

our LCI-MGS inversion.

Seismic surface-wave data were recorded using a Geometrics Geode seismograph with 24 4.5-Hz vertical geophones and a 5-kg sledgehammer as seismic source. The survey was carried out in roll-along mode, i.e., the source and the receiver array are moved together along the profile. The offset between the source and the nearest geophone was kept at 5 m, with a geophone spacing of 1 m, leading to a geophone spread of 23 m. Data were recorded from 67 shot positions with 2-m shot spacing, thus yielding a 132-m long 2D line (Figure 7b-c). For each configuration, the shots were repeated twice and stacked on-site to improve the signal-to-noise ratio. The sampling interval was 0.25 ms, with a record length of 1 s. For each of the configurations, the dispersion curves were picked interactively using either a commercial software (SurfSeis; phasevelocity/frequency domain) (Park et al., 1999) or in-house frequency/wavenumber domain routines. For most parts of the profile, the fundamental Rayleigh mode is dominant (Figure 8a). However, the data covering the south-eastern part of the acquisition line show both fundamental and higher modes (Figure 8b).

The data pseudo-section showing the dispersion curve as a function of the distance from the initial point of the Vålen's survey line is presented in Figure 9. We test four ϵ values ranging from 0.001 to 1 and we use a lateral weight of $\gamma = 2$. Because the observed velocities are slower for this data set, we set a heterogeneous grid composed of 40 layers with a maximum depth of 40 m with the following layer thickness distribution from top to bottom: [10 layers of 0.4 m; 10 layers of 0.8 m; 10 layers of 1.2 m; 10 layers of 1.6 m]. Because we have no robust information about the true level of uncertainties, we assumed, based on the variability in the data, a standard deviation of 2%. The results are shown in Figure 10. Consistently with our assumptions, the large majority of the data are fitted

DOI: 10.1190/geo2021-0247.1

within the 2% threshold; only around 15 Hz, the data misfit is systematically higher, but still it never exceeds 4%.

Not surprisingly, the retrieved shear-wave velocity distributions (characterized by different levels of vertical and lateral of sparsity) are equally compatible with the observations. Still, they present very peculiar and different features; for example, the smooth horizontal transition from the relatively high velocity area (>200 m/s) at the bottom of the section and the shallower layer disappears when the ϵ value decreases. In the same way, also the deepest fast layer is more homogeneous when the inversion settings are selected to favor more blocky reconstructions. In this layer, the geotechnical data indicates a transition between a highly sensitive clay (low β) at the beginning of the profile to less sensitive clay (relatively higher β) towards the middle of the profile. It corroborates the observed β increase from 200 to 250 m/s at 65 m from the beginning of the profile and around 10-15 m depth. Along the same line of reasoning, it is probably worth noticing that the shallow layer ($\sim$150 m/s - characterizing the shear-wave velocity inversion in the near-surface) extends continuously for the entire length of the section in the smoother reconstructions, whereas, when stronger sparsity constraints are chosen, it is not only better defined vertically, but, laterally, it dissolves into an (almost) homogeneous upper layer of (<150 m/s). The interpretation of the geotechnical soundings available for this test site indicates the presence of a quick-clay layer from about 30 m distance to the end of the line, at about 5 m depth. This unit is around 10 m towards the end of the profile and thinner in the middle. The low velocity layer around 5 m below surface would then correspond to the quick clay. To this respect, the inversion results with a low ϵ value are in better agreement with the interpretation of the geotechnical soundings. The more detailed correspondence of the different inversion results with the actual geology needs to be further investigated, but it is, in any case, not

the point of the present research. In fact, what we would like to convey here is that surface wave inversion is a severely ill-posed problem, so, a proper regularization is necessary and the MGS provides a useful tool to explore the model space by enforcing variable levels of sparsity both in the vertical and, now, also the horizontal directions.

CONCLUSION

We incorporate the Minimum Gradient Support (MGS) regularization into a Laterally Constrained Inversion (LCI) of seismic surface wave data. This allows the reconstruction of (pseudo-)2D distribution of shear-wave velocity inferred from dispersion curve measurements with a tunable level of sparsity. It is the first time that LCI-MGS approaches are applied to seismic surface wave inversion. The adopted strategy for the automatic selection of the parameter controlling the importance of the regularization is discussed in detail. The performances of this novel algorithm are tested both on synthetic and field data showing, once more, the necessity for a flexible tool to explore the solution space and to enforce the model spatial coherence by means of the proper prior information. In this respect, the field example illustrates that even with a relatively low noise level in the data, rather different shear-wave velocity distributions can be inferred. This variability needs to be taken into account and possibly quantified in order to support quantitatively decisions that might have relevant socio-economic impacts, as, here, concerning the quick clay conditions, or in other cases, regarding, for example, the seismic risk assessment. Finally, our approach can be extended to 3D data sets by including similar model constraints in the cross-line direction.

DOI: 10.1190/geo2021-0247.1

ACKNOWLEDGEMENTS

This work was partially supported by the Deutsche Forschungsgemeinschaft (DFG) (grant number 418056756) and by *Regione Autonoma della Sardegna (Legge regionale 7 agosto 2007, n.7 "Promozione della Ricerca Scientifica e dell'Innovazione Tecnologica in Sardegna")* through the *Programma di mobilità dei giovani ricercatori 2018*; by the project GEO-CUBE (CUP F72F20000250007). In addition, Giulio Vignoli and Jeniffer Barreto are grateful to LABMAST (University of Cagliari), and, particularly, to Antonio Cazzani and Sergio De Montis for their help.

DATA AND MATERIALS AVAILABILITY

The inversion program presented in this study can be provided by the corresponding author upon reasonable request.

REFERENCES

Aster, R. C., B. Borchers, and C. H. Thurber, 2005, Parameter estimation and inverse problems: Elsevier.

Auken, E., and A. V. Christiansen, 2004, Layered and laterally constrained 2d inversion of resistivity data: Geophysics, **69**, 752–761.

Auken, E., A. V. Christiansen, B. H. Jacobsen, N. Foged, and K. I. Sorensen, 2005, Piecewise 1D laterally constrained inversion of resistivity data: Geophysical Prospecting, **53**, 497–506.

Bergamo, P., D. Boiero, and L. V. Socco, 2012, Retrieving 2d structures from surface-wave data by means of space-varying spatial windowing: Geophysics, **77**, EN39–EN51.

Boaga, J., S. Renzi, G. Vignoli, R. Deiana, and G. Cassiani, 2012, From surface wave inversion to seismic site response prediction: Beyond the 1d approach: Soil Dynamics and Earthquake Engineering, **36**, 38–51.

Brown, V., K. Key, and S. Singh, 2012, Seismically regularized controlled-source electromagnetic inversion: Geophysics, **77**, E57–E65.

Constable, S. C., R. L. Parker, and C. G. Constable, 1987, Occams inversion: a practical algorithm for generating smooth models from electromagnetic sounding data: Geophysics, **52**, 289–300.

Craig, M. S., K. Hayashi, and Ö. Kozacı, 2021, Active and passive seismic surface wave methods for levee assessment in the sacramento-san joaquin delta, california, usa: Near Surface Geophysics.

Da Col, F., M. Papadopoulou, E. Koivisto, Ł. Sito, M. Savolainen, and L. V. Socco, 2020, Application of surface-wave tomography to mineral exploration: a case study from siilinjärvi, finland: Geophysical Prospecting, **68**, 254–269.

deGroot Hedlin, C., and S. Constable, 1990, Occam's inversion to generate smooth, two-dimensional models from magnetotelluric data: Geophysics, **55**, 1613–1624.

Esfahani, R. D. D., A. Gholami, and M. Ohrnberger, 2020, An inexact augmented Lagrangian method for nonlinear dispersion curve inversion using Dix-type global linear approximation: Geophysics, **85**, 1–38.

Farrugia, D., E. Paolucci, S. D'Amico, and P. Galea, 2016, Inversion of surface wave data for subsurface shear wave velocity profiles characterized by a thick buried low-velocity layer: Geophysical Journal International, **206**, 1221–1231.

Foti, S., and C. Strobbia, 2002, Some notes on model parameters for surface wave data inversion: 15th EEGS Symposium on the Application of Geophysics to Engineering and Environmental Problems, European Association of Geoscientists & Engineers, cp–191.

Halliday, D. F., A. Curtis, P. Vermeer, C. Strobbia, A. Glushchenko, D.-J. van Manen, and J. O. Robertsson, 2010, Interferometric ground-roll removal: Attenuation of scattered surface waves in single-sensor data: Geophysics, **75**, SA15–SA25.

Haney, M. M., and L. Qu, 2010, Rayleigh wave dispersion curve inversion: Occam versus the l1-norm, *in* SEG Technical Program Expanded Abstracts 2010: Society of Exploration Geophysicists, 1871–1876.

Haney, M. M., and V. C. Tsai, 2017, Perturbational and nonperturbational inversion of Rayleigh-wave velocities: Geophysics, **82**, F15–F28.

Key, K., 2016, Mare2dem: a 2-d inversion code for controlled-source electromagnetic and magnetotelluric data: Geophysical Journal International, **207**, 571–588.

Lysmer, J., 1970, Lumped mass method for rayleigh waves: Bulletin of the Seismological Society of America, **60**, 89–104.

Park, C. B., R. D. Miller, and J. Xia, 1999, Multichannel analysis of surface waves: Geo-

physics, **64**, 800–808.

Pfaffhuber, A., M. Bastani, S. Cornée, M. Rømoen, S. Donohue, T. Helle, M. Long, P. O'Connor, and L. Persson, 2010, Multi-method high resolution geophysical & geotechnical quick clay mapping: Near Surface 2010-16th EAGE European Meeting of Environmental and Engineering Geophysics, European Association of Geoscientists & Engineers, cp–164.

Portniaguine, O., and M. S. Zhdanov, 1999, Focusing geophysical inversion images: Geophysics, **64**, 874–887.

Sauvin, G., S. Bazin, M. Vanneste, I. Lecomte, and A. Pfaffhuber, 2011, Towards joint inversion/interpretation for landslide-prone areas in norway-integrating geophysics and geotechnique: Near Surface 2011-17th EAGE European Meeting of Environmental and Engineering Geophysics, European Association of Geoscientists & Engineers, cp–253.

Socco, L. V., D. Boiero, S. Foti, and R. Wisén, 2009, Laterally constrained inversion of ground roll from seismic reflection records: Geophysics, **74**, G35–G45.

Vignoli, G., G. Cassiani, M. Rossi, R. Deiana, J. Boaga, and P. Fabbri, 2012, Geophysical characterization of a small pre-alpine catchment: Journal of applied geophysics, **80**, 32–42.

Vignoli, G., G. Fiandaca, A. V. Christiansen, C. Kirkegaard, and E. Auken, 2015, Sharp spatially constrained inversion with applications to transient electromagnetic data: Geophysical Prospecting, **63**, 243–255.

Vignoli, G., I. Gervasio, G. Brancatelli, J. Boaga, B. Della Vedova, and G. Cassiani, 2016, Frequency-dependent multi-offset phase analysis of surface waves: an example of high-resolution characterization of a riparian aquifer: Geophysical Prospecting, **64**, 102–111.

Vignoli, G., J. Guillemoteau, J. Barreto, and M. Rossi, 2021, Reconstruction, with tunable sparsity levels, of shear wave velocity profiles from surface wave data: Geophysical Journal

International, **225**, 1935–1951.

Vignoli, G., V. Sapia, A. Menghini, and A. Viezzoli, 2017, Examples of improved inversion of different airborne electromagnetic datasets via sharp regularization: Journal of Environmental and Engineering Geophysics, **22**, 51–61.

Vignoli, G., C. Strobbia, G. Cassiani, and P. Vermeer, 2011, Statistical multioffset phase analysis for surface-wave processing in laterally varying media: Geophysics, **76**, U1–U11.

Wang, J., and T.-L. Teng, 1994, Surface wave profiling of the lithosphere beneath the mojave desert using terrascope data: Journal of Geophysical Research: Solid Earth, **99**, 743–750.

Wathelet, M., 2008, An improved neighborhood algorithm: parameter conditions and dynamic scaling: Geophysical Research Letters, **35**.

Wathelet, M., D. Jongmans, and M. Ohrnberger, 2004, Surface-wave inversion using a direct search algorithm and its application to ambient vibration measurements: Near surface geophysics, **2**, 211–221.

Wisén, R., and A. V. Christiansen, 2005, Laterally and mutually constrained inversion of surface wave seismic data and resistivity data: Journal of Environmental & Engineering Geophysics, **10**, 251–262.

Xia, J., R. D. Miller, and C. B. Park, 1999, Estimation of near-surface shear-wave velocity by inversion of rayleigh waves: Geophysics, **64**, 691–700.

Xing, G., F. Niu, M. Chen, and Y. Yang, 2016, Effects of shallow density structure on the inversion for crustal shear wave speeds in surface wave tomography: Geophysical Journal International, **205**, 1144–1152.

Yan, P., T. Kalscheuer, P. Hedin, and M. A. Garcia Juanatey, 2017, Two-dimensional magnetotelluric inversion using reflection seismic data as constraints and application in

DOI: 10.1190/geo2021-0247.1

the COSC project: Geophysical Research Letters, **44**, 3554–3563.

FIGURE CAPTIONS

Figure1. Description of the inverse modelling algorithm. a) Homogeneous subsurface background model with two local perturbations in shear-wave velocity. b) Comparison between J (equation 1) and G (equation 3) gradients computed for the model shown in a), and for the frequency $f = 15$ Hz. The results highlights how G is less dependent on the perturbations shown in a), which means that the related inverse problem is more comparable to a linear inverse problem. c) Strategy for selecting the model regularization weight at each iteration of the Occam procedure. d) Description of the decoupling between the FE grid used for forward calculations and the (coarser) parameter grid defined for the inversion.

Figure 2. Noise free synthetic experiment with $\epsilon = 0.001$ for two different parameter grids. a) Comparison between the models resulting from the inversions and the true model used for computing the synthetic data. b) Observed versus modelled data for the two tests. c) Data misfits in term of relative RMS error. d) Evolution of the misfit during the iterative inverse procedure. Layer thickness in meter for the 2 grids from top to bottom: homogeneous grid of 550 layers up to a depth of 110 m [550×0.2 m], heterogeneous grid of 100 layers up to 110 m [10 layers of 0.2 m; 10 layers of 0.4 m; 10 layers of 0.6 m; 10 layers of 0.8 m; 10 layers of 1.0 m; 10 layers of 1.2 m; 10 layers of 1.4 m; 10 layers of 1.6 m; 10 layers of 1.8 m; 10 layers of 2 m].

Figure 3. Noisy ($\pm 5\%$) synthetic experiment using the heterogeneous grid considered in the previous figure (100 layers) for $\epsilon = 0.001$ (sharp) and $\epsilon = 1$ (smooth). a) Comparison between the models obtained from both sharp and smooth inversions and the true model used for computing the synthetic data. b) Observed versus modelled data for the two tests. c) Data misfits in term of relative RMS error. d) Evolution of the misfits during the iterative inverse procedure. We use a heterogeneous parameter grid with layer thickness increasing with depth and detailed in Figure 2.

DOI: 10.1190/geo2021-0247.1

Figure 4. Synthetic pseudo-section composed of 50 soundings with (±5%) uncorrelated noise. a) Noisy synthetic multi-sounding data set. b) Input 1D subsurface $\boldsymbol{\beta}$ models stitched along the pseudo-section. The physical properties of the different layers are summarized in Table 1.

Figure 5. Single-sounding MGS inversions for different value of ϵ applied to a pseudo-2D noisy (±5%) profile. a) Relative RMS value for each data point. b) Mean relative RMS value for each sounding. c) Pseudo-2D model resulting from stitching all the 1D inversion results along the pseudo-section. The used inversion grid is the same heterogeneous one utilized for the results in Figures 2 and 3. The white dashed line represents the interfaces of the true models. Note that because only single-sounding inversions were performed for this test, we do not provide a global mean relative RMS misfit value for the entire profile.

Figure 6. Multi-sounding MGS inversions for different values of ϵ and $\gamma = 0.5$ applied to a pseudo-2D noisy (±5%) profile. a) Relative RMS value for each datum; the global relative RMS value is indicated above the graphics. b) Mean relative RMS value for each sounding. c) Pseudo-2D section resulting from stitching all the 1D inversion results along the pseudo-line. The used inversion grid is the same heterogeneous one utilized for the results in Figures 2, 3 and 5. The white dashed line represents the interfaces of the true models.

Figure 7. a) Location of the Vålen quick clay test site. b) Location of the MASW profile and the two arrays used for collecting shots gathers 12 and 67, which are shown in Figure 8. c) Schematic description of the survey deployment (stars: shots, dots: receivers).

Figure 8. Space-time (left) and frequency-wavenumber (right) analysis of a) shot gather 12 and b) shot gather 67. The spectra show that mode contaminations are not affecting the data. The western part (e.g., shot gather 12) of the profile only shows the fundamental mode and the eastern part (e.g., shot gather 67) shows the fundamental and the first harmonic modes.

Figure 9. Pseudo-section of the Rayleigh wave velocity as function of frequency and off-set

as extracted in the range 5-50 Hz, from seismic data collected in Vålen (Norway). Each column represents the dispersion curve for that specific location.

Figure 10. Multi-sounding MGS inversions for different values of ϵ and $\gamma = 2$ applied to the field data shown in Figure 9. a) Relative RMS value for each data point; the global relative RMS value is indicated above the graphics. b) Mean relative RMS value for each sounding. c) Pseudo-2D section resulting from stitching all the 1D inversion results along the pseudo-line. We use a 40 layers heterogeneous parameter grid with layer thickness varying from top to bottom as follows: [10 layers of 0.4 m; 10 layers of 0.8 m; 10 layers of 1.2 m; 10 layers of 1.6 m].

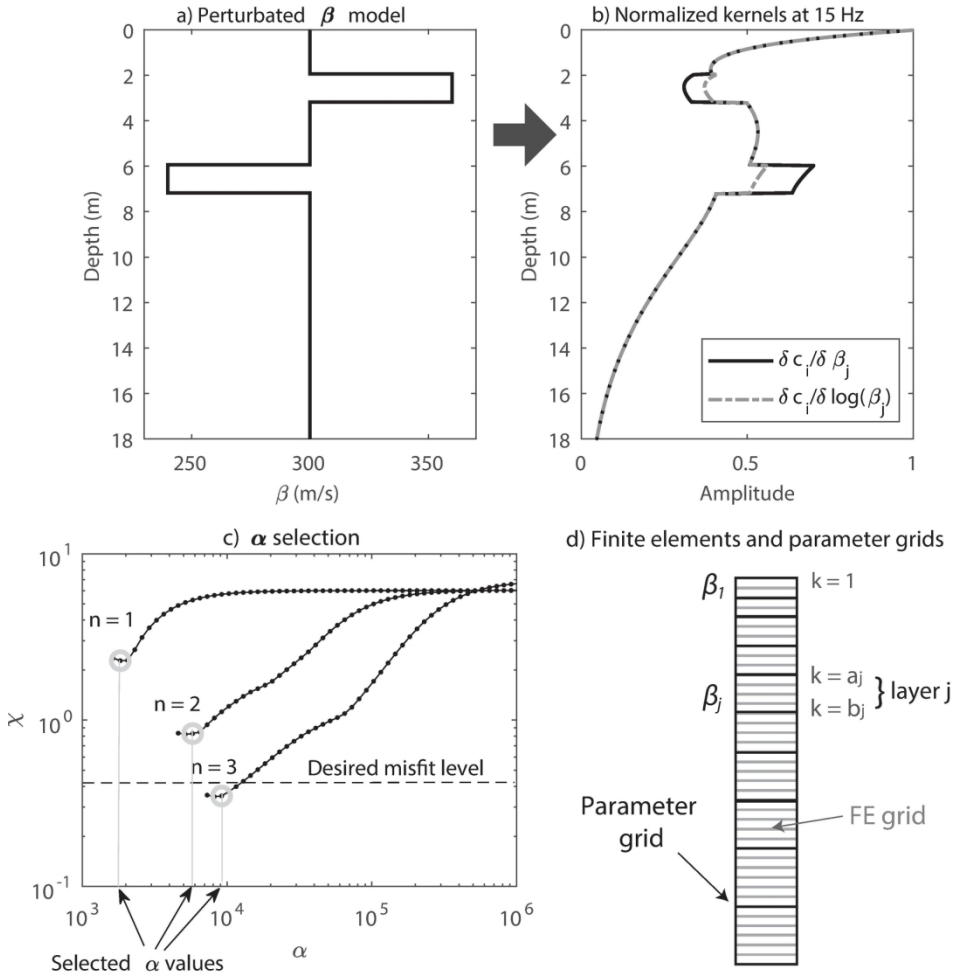

Figure 1.Description of the inverse modelling algorithm. a) Homogeneous subsurface background model with two local perturbations in shear-wave velocity. b) Comparison between *J* (equation 1) and *G* (equation 3) gradients computed for the model shown in a), and for the frequency *f* = 15 Hz. The results highlights how *G* is less dependent on the perturbations shown in a), which means that the related inverse problem is more comparable to a linear inverse problem. c) Strategy for selecting the model regularization weight at each iteration of the Occam procedure. d) Description of the decoupling between the FE grid used for forward calculations and the (coarser) parameter grid defined for the inversion.

157x155mm (300 x 300 DPI)

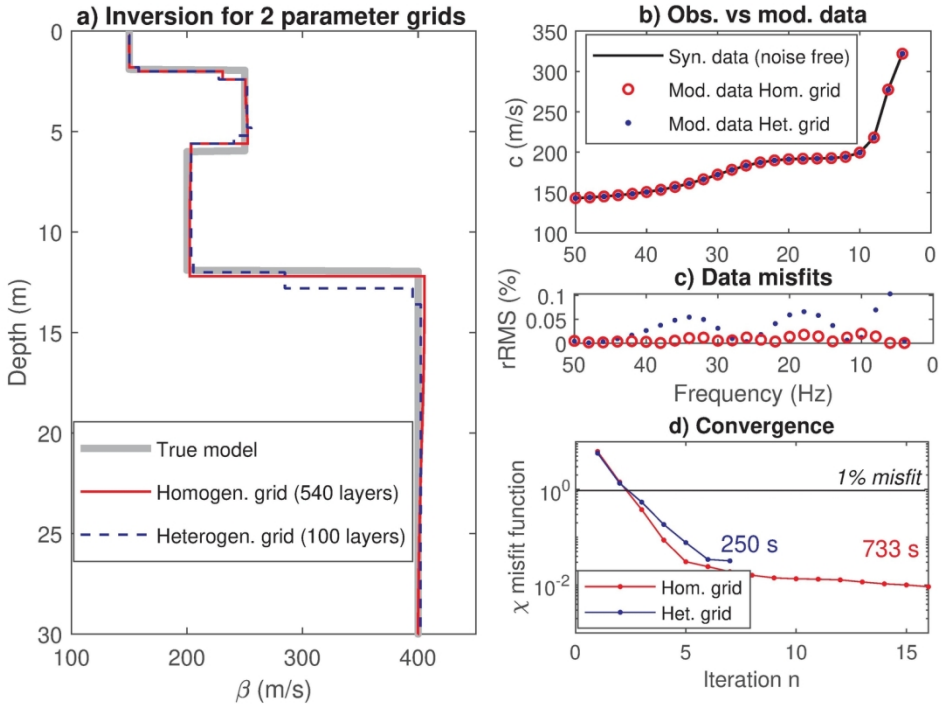

Figure 2. Noise free synthetic experiment with ☐ = 0.001 for two different parameter grids. a) Comparison between the models resulting from the inversions and the true model used for computing the synthetic data. b) Observed versus modelled data for the two tests. c) Data misfits in term of relative RMS error. d) Evolution of the misfit during the iterative inverse procedure. Layer thickness in meter for the 2 grids from top to bottom: homogeneous grid of 550 layers up to a depth of 110 m [550 × 0.2 m], heterogeneous grid of 100 layers up to 110 m [10 layers of 0.2 m; 10 layers of 0.4 m; 10 layers of 0.6 m; 10 layers of 0.8 m; 10 layers of 1.0 m; 10 layers of 1.2 m; 10 layers of 1.4 m; 10 layers of 1.6 m; 10 layers of 1.8 m; 10 layers of 2 m].

150x111mm (300 x 300 DPI)

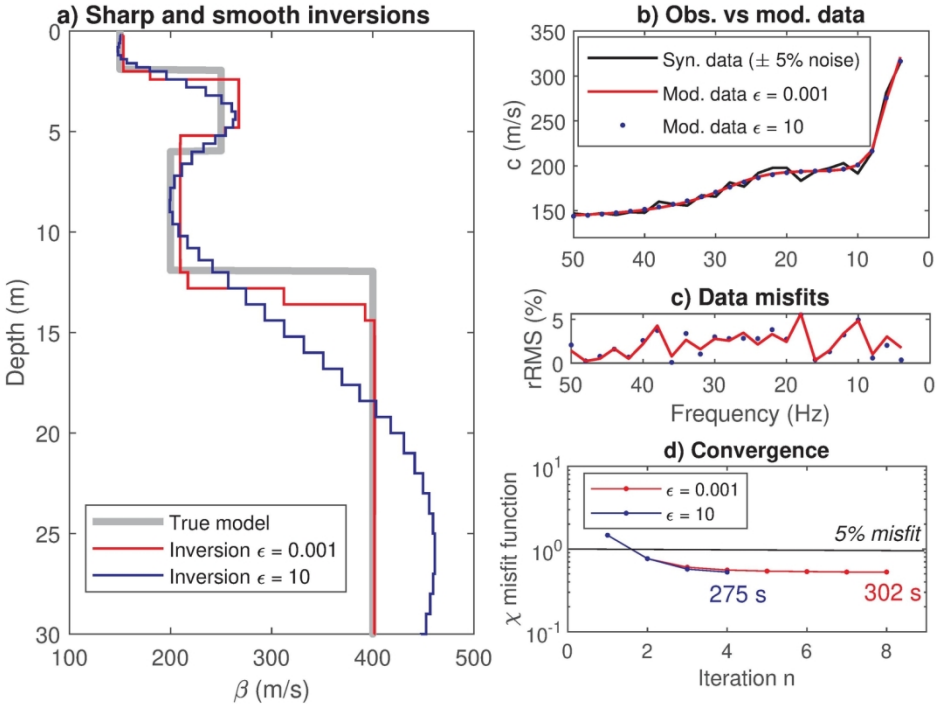

Figure 3. Noisy (±5%) synthetic experiment using the heterogeneous grid considered in the previous figure (100 layers) for □ = 0.001 (sharp) and □ = 1 (smooth). a) Comparison between the models obtained from both sharp and smooth inversions and the true model used for computing the synthetic data. b) Observed versus modelled data for the two tests. c) Data misfits in term of relative RMS error. d) Evolution of the misfits during the iterative inverse procedure. We use a heterogeneous parameter grid with layer thickness increasing with depth and detailed in Figure 2.

150x111mm (300 x 300 DPI)

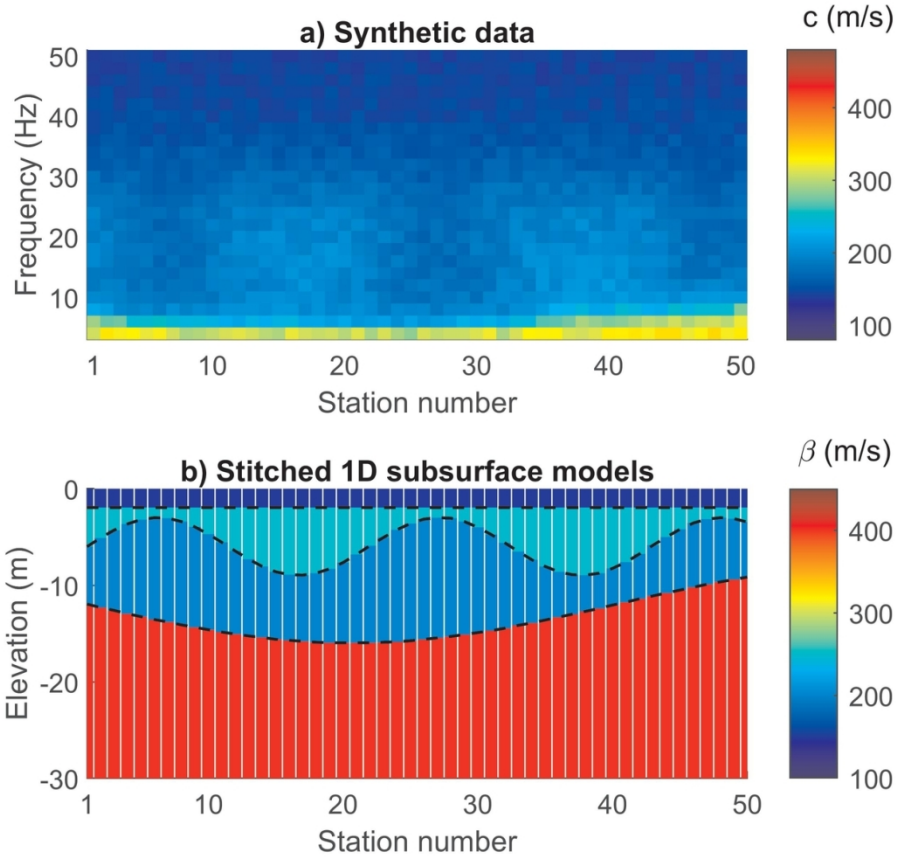

Figure 4. Synthetic pseudo-section composed of 50 soundings with (±5%) uncorrelated noise. a) Noisy synthetic multi-sounding data set. b) Input 1D subsurface β models stitched along the pseudo-section. The physical properties of the different layers are summarized in Table 1.

118x104mm (300 x 300 DPI)

DOI: 10.1190/geo2021-0279.1

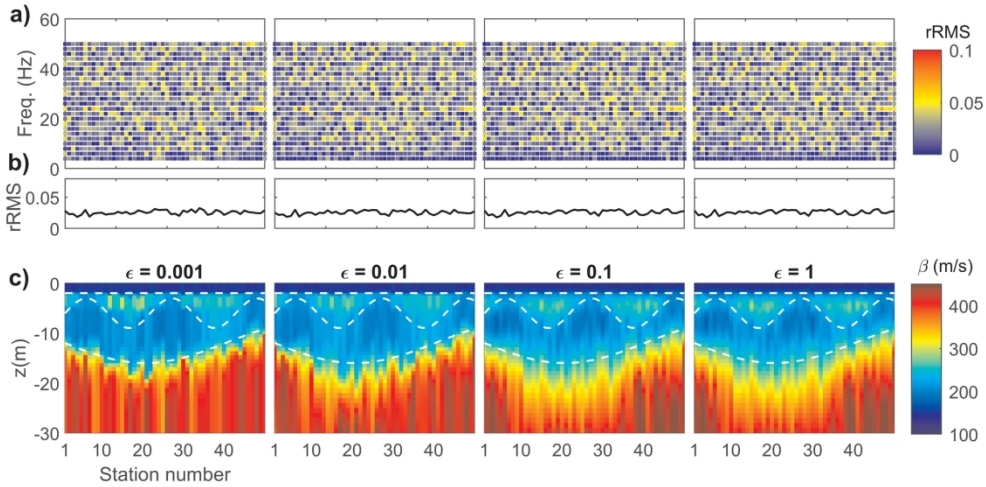

Figure 5. Single-sounding MGS inversions for different value of ☐ applied to a pseudo-2D noisy (±5%) profile. a) Relative RMS value for each data point. b) Mean relative RMS value for each sounding. c) Pseudo-2D model resulting from stitching all the 1D inversion results along the pseudo-section. The used inversion grid is the same heterogeneous one utilized for the results in Figures 2 and 3. The white dashed line represents the interfaces of the true models. Note that because only single-sounding inversions were performed for this test, we do not provide a global mean relative RMS misfit value for the entire profile.

180x89mm (300 x 300 DPI)

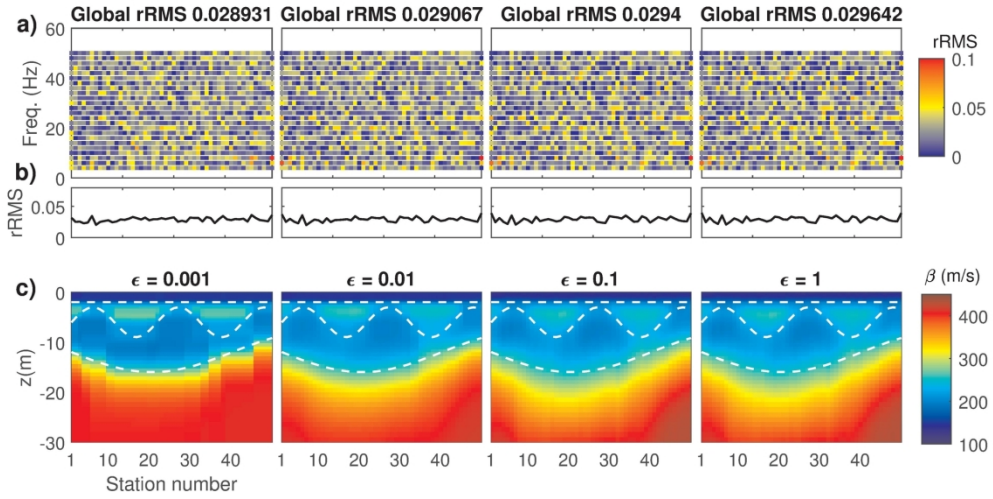

Figure 6. Multi-sounding MGS inversions for different values of ☐ and γ = 0.5 applied to a pseudo2D noisy (±5%) profile. a) Relative RMS value for each datum; the global relative RMS value is indicated above the graphics. b) Mean relative RMS value for each sounding. c) Pseudo-2D section resulting from stitching all the 1D inversion results along the pseudo-line. The used inversion grid is the same heterogeneous one utilized for the results in Figures 2, 3 and 5. The white dashed line represents the interfaces of the true models.

180x89mm (300 x 300 DPI)

DOI: 10.1190/geo2021-0279.1

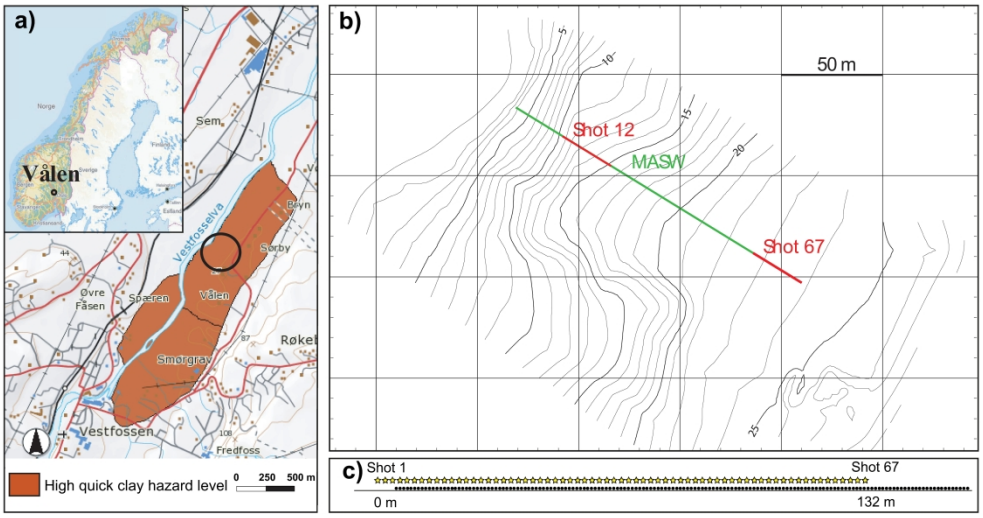

Figure 7. a) Location of the Vålen quick clay test site. b) Location of the MASW profile and the two arrays used for collecting shots gathers 12 and 67, which are shown in Figure 8. c) Schematic description of the survey deployment (stars: shots, dots: receivers).

524x282mm (300 x 300 DPI)

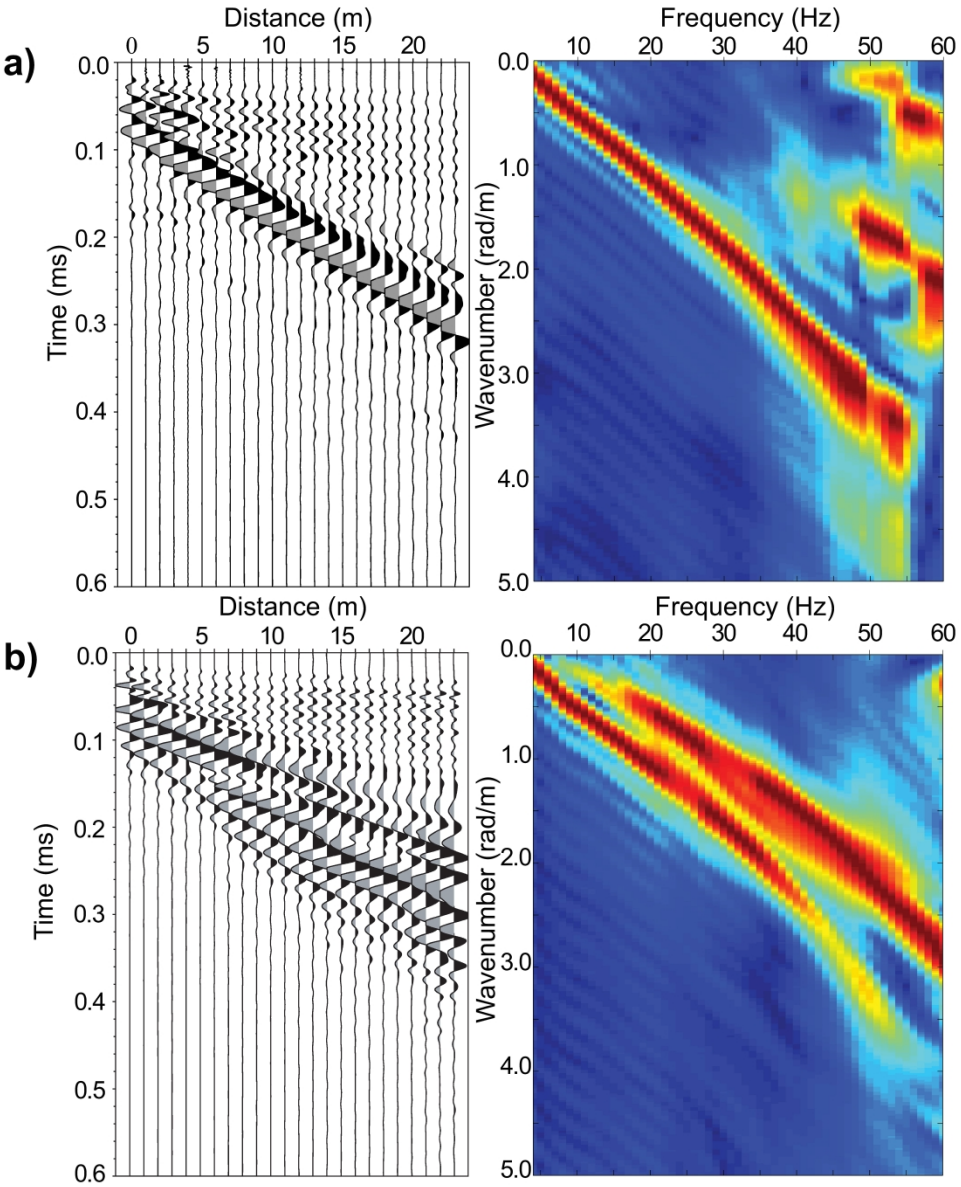

Figure 8. Space-time (left) and frequency-wavenumber (right) analysis of a) shot gather 12 and b) shot gather 67. The spectra show that mode contaminations are not affecting the data. The western part (e.g., shot gather 12) of the profile only shows the fundamental mode and the eastern part (e.g., shot gather 67) shows the fundamental and the first harmonic modes.

400x484mm (600 x 600 DPI)

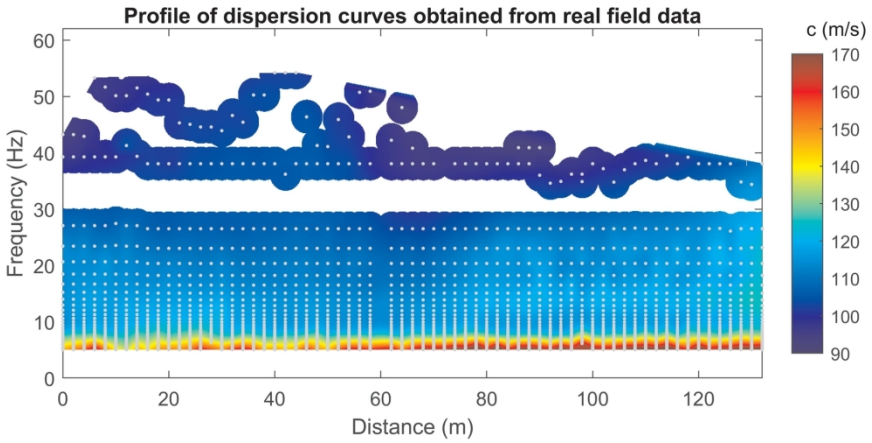

Figure 9. Pseudo-section of the Rayleigh wave velocity as function of frequency and off-set as extracted in the range 5-50 Hz, from seismic data collected in Vålen (Norway). Each column represents the dispersion curve for that specific location.

180x89mm (300 x 300 DPI)

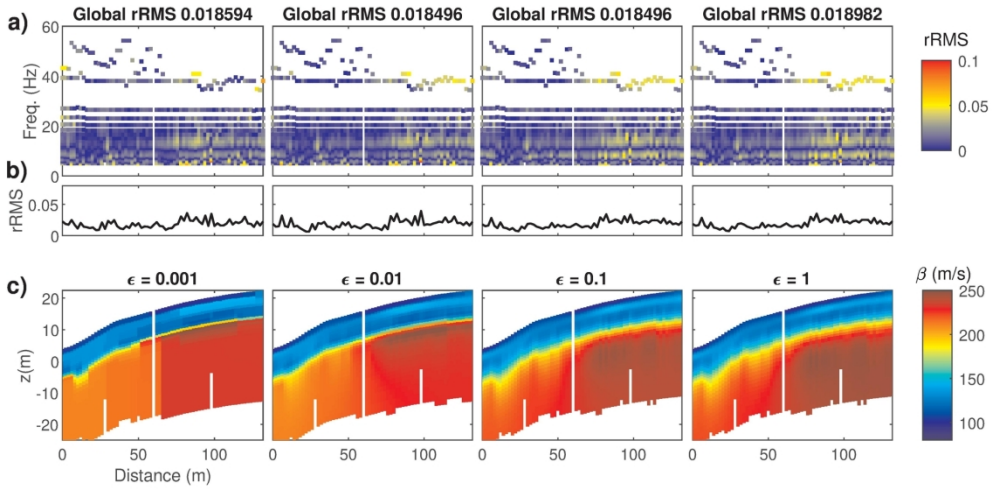

Figure 10. Multi-sounding MGS inversions for different values of ☐ and γ = 2 applied to the field data shown in Figure 9. a) Relative RMS value for each data point; the global relative RMS value is indicated above the graphics. b) Mean relative RMS value for each sounding. c) Pseudo-2D section resulting from stitching all the 1D inversion results along the pseudo-line. We use a 40 layers heterogeneous parameter grid with layer thickness varying from top to bottom as follows: [10 layers of 0.4 m; 10 layers of 0.8 m; 10 layers of 1.2 m; 10 layers of 1.6 m].

180x89mm (300 x 300 DPI)

Layer	α (m/s)	β (m/s)	ρ (kg.m^3)	h (m)
1	260	150	1.24	2
2	433	250	1.41	4
3	346	200	1.35	6
4	693	400	1.57	∞

Table 1: Model used for the single sounding synthetic tests; the shear-wave vertical distribution is equal to the one of "Model 2" in Esfahani et al. (2020).

DATA AND MATERIALS AVAILABILITY

Custom statement of data and materials availability

DOI:10.1190/geo2021-0247.1